

# Efficiency Increase in Multijunction Monochromatic Photovoltaic Devices Due to Luminescent Coupling

Daixi Xia<sup>1</sup> and Jacob J. Krich<sup>1,2</sup>

<sup>1</sup>*Department of Physics, University of Ottawa, Ottawa, Canada*

<sup>2</sup>*School of Electrical Engineering and Computer Science, University of Ottawa, Ottawa, Canada*

(Dated: April 2, 2020)

We present a multijunction detailed balance model that includes the effects of luminescent coupling, light trapping and nonradiative recombination, suitable for treatment of multijunction solar cells and photonic power converters – photovoltaic devices designed to convert narrow-band light. The model includes both specular and Lambertian reflections using a ray-optic formalism and treats nonradiative processes using an internal radiative efficiency. Using this model, we calculate and optimize the efficiency of multijunction photonic power converters for a range of material qualities and light-trapping schemes. Multijunction devices allow increased voltage with lower current, decreasing series resistance losses. We show that efficiency increases significantly with increased number of junctions, even without series resistance, when the device has an absorbing substrate. Such an increase does not occur when the device has a back reflector. We explain this effect using a simplified model, which illustrates the origin of the decreased radiative losses in multijunction devices on substrates.

## I. INTRODUCTION

In both solar and monochromatic photovoltaics, it is well-known that a multijunction device reduces series-resistance loss compared to a single-junction equivalent, because of the low-current, high-voltage operation. High efficiency devices also rely on both photon recycling within a layer and luminescent coupling (LC) between layers, effects that are essential to accurate prediction of device performance. Monochromatic photovoltaics, also called photonic power converters (PPC's), are increasingly important components of optical power transmission systems. LC has been well studied in solar cells<sup>1-5</sup> and has been implemented in a drift-diffusion solver for PPC's<sup>6</sup>. There is, however, no previous detailed-balance model including LC in multijunction PPC's. Though these photovoltaic technologies are similar, there is a crucial difference between LC in solar cells and in PPC's: in solar cells, internally emitted photons can only be absorbed in the layers with lower bandgaps, so LC is one-directional; in PPC's, because all layers have the same band gap, LC is bi-directional. Previous LC models also treat only specular reflections.

High-efficiency PPC's enable wireless power transmission isolated from electromagnetic disturbance, with applications in electric vehicles, biomedical implants, telecommunications, drones, and satellites<sup>7-10</sup>. The record-efficiency PPC is a vertical multijunction structure with 5 GaAs pn junctions coupled with tunnel diodes; it obtained an efficiency of 70% and operating voltage of greater than 5 V at an input power density of 8 W/cm<sup>2</sup><sup>11</sup>. Even without consideration of series resistance, increased voltage is desirable in applications because of the removal of the need to boost the voltage. In this work, we use the term “layers” to refer to the active absorbing pn junctions, to avoid confusing these absorbing junctions with tunnel diodes, which are often called

tunnel junctions.

In 2001, Green used the detailed-balance formalism to show that monochromatic photovoltaic conversion can be 100% efficient at infinite incident intensity<sup>12</sup>. Green's theory is a single-layer model, which does not capture the low current, high voltage of multi-layer operation and does not consider LC in a multi-layer device. In this work, we extend Green's theory to a multi-layer detailed-balance model and include bidirectional LC. Our model treats both specular and Lambertian top and bottom surfaces, variable incident light bandwidth, energy offset between incident light and material band gap, and nonradiative recombination by parametrizing with an internal radiative efficiency  $\eta_{\text{int}}$ . We use this model to study a range of devices based on the record-efficiency PPC<sup>11</sup>, showing the efficiency potential for future device architectures. We show that PPC efficiency increases with the number of layers, even without series-resistance loss, when the device has an absorbing substrate. This effect is not present for devices with a back reflector. We explain the origin of this effect using a simple analytic 2-layer model. This model also enables study of multijunction solar cells, with flexible application to include light trapping top and bottom surfaces.

Section II introduces the detailed balance model for a 1-layer device, including treatment of reflections from top and bottom surfaces. Section III extends this theory to the multi-layer case. Section IV shows how to transform the nonlinear equations for current  $J$  as a function of voltage  $V$  into a set of linear equations that allow computationally efficient extraction of  $V(J)$ . Section V applies the multi-layer theory to PPC's with a range of  $\eta_{\text{int}}$  values and light-trapping configurations, showing the intrinsic efficiency increase with number of layers when the device has an absorbing substrate. Section VI explains the intrinsic efficiency increase using an analytic 2-layer model.

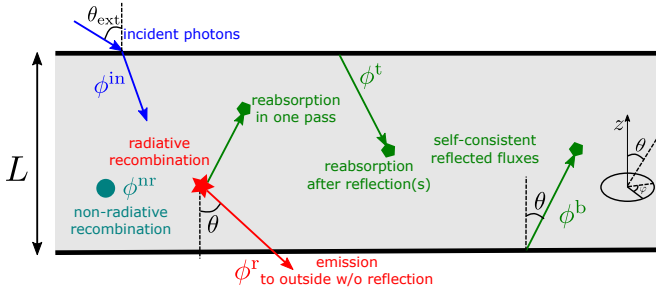


Figure 1. Absorption and recombination events in a single-layer cell.

## II. SINGLE-LAYER DETAILED BALANCE

We model a planar cell with infinite area and finite thickness  $L$  of the active region, as shown in Fig. 1. The detailed balance condition in this cell is

$$J = J^{\text{in}} - J^{\text{loss}}, \quad (1)$$

where  $J$  is the extracted current density,  $J^{\text{in}}$  is the number of incident photons absorbed per area per time,  $J^{\text{loss}}$  is the net loss of current density due to electron-hole recombination, and we set the electric charge  $q = 1$ .  $J^{\text{loss}}$  is a function of the quasi-Fermi level separation  $\mu$ , described further below. We make standard detailed balance assumptions that carrier mobilities are infinite so  $\mu$  equals the applied voltage and that one photon generates one electron-hole pair<sup>13</sup>. The efficiency of the device is:

$$\eta(\mu) = \frac{J(\mu)\mu}{P_{\text{in}}} \quad (2)$$

where  $P_{\text{in}}$  is the incident power density. The maximum efficiency is obtained by optimizing  $\eta$  with respect to  $\mu$ .

To model both  $J^{\text{in}}$  and  $J^{\text{loss}}$ , we trace the absorption and emission of photons using ray optics. We use an angle-resolved 2D model, isotropic in the azimuth, suitable for layered structures. As shown in Fig. 1,  $\theta$  is the angle between the direction of propagation of the photons and the normal of the cell, defined from 0 to  $\pi/2$ . When the top or bottom surfaces have specular reflections, photons with angle  $\theta$  are coupled to those with angle  $\pi - \theta$ , and we label these populations with  $\theta \in [0, \pi/2]$ . Alternatively, a Lambertian surface couples photon populations of all angles to each other.

The only challenging part of evaluating Eq. 1 lies in keeping track of the reflections off the top and bottom surfaces, both from incident and radiatively produced radiation. Both of these processes share the same algebraic form, and we now describe the resulting self-consistency condition including reflections.

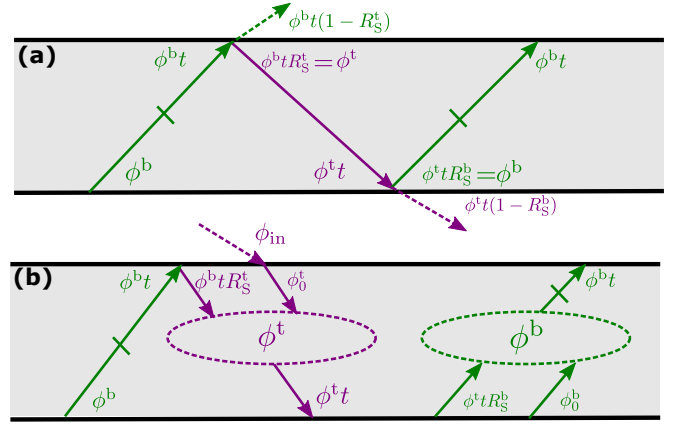


Figure 2. Self-consistency relation between top and bottom inward photon fluxes,  $\phi^t(\theta, E)$ , and  $\phi^b(\theta, E)$ , (a) without source terms and (b) with source terms  $\phi_0^t(\theta, E)$  and  $\phi_0^b(\theta, E)$ . Figure shows specular top and bottom surfaces. In the case where the source is from external radiation  $\phi_{\text{in}}$ ,  $\phi_0^t = \phi_{\text{in}}(1 - R_{\text{ext}})$ .

### A. Self-Consistency Condition for Reflections

Consider the inward-directed photon fluxes from the top and bottom surfaces with angle  $\theta$  and energy  $E$ ,  $\phi^t(\theta, E)$ , and  $\phi^b(\theta, E)$ , respectively. A self-consistency relation connects these quantities; it was used to model photon recycling – reabsorption of internally emitted photons in a single-layer device – in Ref.<sup>14</sup> with specular reflection. Here, we exploit this self-consistency relation to model both photon recycling in single-layer structures and luminescent coupling in multi-layer structures and extend it to include Lambertian reflections.

Consider first specular reflections from top and bottom surfaces. As shown in Fig. 2, the inward photon flux at one surface must be equal to the flux at the opposite surface that is transmitted through the entire cell and reflects at the considered surface. This relation is expressed as:

$$\phi^t(\theta, E) = \phi^b(\theta, E) t(\theta, E) R_S^t(\theta, E) \quad (3)$$

$$\phi^b(\theta, E) = \phi^t(\theta, E) t(\theta, E) R_S^b(\theta, E) \quad (4)$$

where  $R_S^t(\theta, E)$  and  $R_S^b(\theta, E)$  are internal specular reflectivity at the top and bottom surface, respectively. We also define  $\theta$ - and  $E$ -resolved transmittance and absorbance:

$$t(\theta, E) = e^{-\frac{\alpha(E)L}{\cos\theta}} \quad (5)$$

$$a(\theta, E) = 1 - t(\theta, E) \quad (6)$$

where  $\alpha(E)$  is the absorption coefficient, which we assume to be uniform in space inside the cell. Eqs. (3), (4) can be read from Fig. 2(a). As written, they have only the trivial solution  $\phi^t = \phi^b = 0$ , but they express the

self-consistency condition that still applies when sources such as external radiation or radiative recombination are included. See below, Eqs. 11, 12. We also construct this self-consistency relation with one or two Lambertian surfaces present. A Lambertian surface is an ideal diffuse scatterer that randomizes the angle of reflected and transmitted rays<sup>15?</sup>. Because all photons travel at random angles, the important quantity is the  $\theta$ -averaged flux,  $\Phi^t(E)$ , and  $\Phi^b(E)$ :

$$\Phi^t(E) = \int_0^{\pi/2} \sin\theta' d\theta' \phi^t(\theta', E) \quad (7)$$

$$\Phi^b(E) = \int_0^{\pi/2} \sin\theta' d\theta' \phi^b(\theta', E) \quad (8)$$

From the Lambert cosine law, the  $\theta$ -resolved fluxes are related to the  $\theta$ -averaged fluxes as<sup>2</sup>:

$$\phi^t(\theta, E) = 2\cos\theta\Phi^t(E) \quad (9)$$

$$\phi^b(\theta, E) = 2\cos\theta\Phi^b(E) \quad (10)$$

Therefore, combining Eqs. 3, 4 and 7 to 10,

$$\phi^t(\theta, E) = 2\cos\theta \int_0^{\pi/2} \sin\theta' d\theta' \phi^b(\theta', E) t(\theta', E) R_L^t(E)$$

$$\phi^b(\theta, E) = 2\cos\theta \int_0^{\pi/2} \sin\theta' d\theta' \phi^t(\theta', E) t(\theta', E) R_L^b(E)$$

where  $R_L^t(E)$  and  $R_L^b(E)$  are  $E$ -resolved Lambertian reflectivities of the top and bottom surfaces, respectively.

Internal and external sources of photons add to these self-consistent fluxes, as shown in Fig. 2(b). We express the inward-directed source at the top and bottom surfaces as  $\phi_0^t(\theta, E)$  and  $\phi_0^b(\theta, E)$ , respectively. With these sources, the self-consistency conditions at top and bottom are:

$$\text{Specular : } \phi^t = \phi^b t R_S^t + \phi_0^t \quad (11a)$$

$$\text{Lambertian : } \phi^t = 2\cos\theta \int_0^{\pi/2} \sin\theta' d\theta' (\phi^b t R_L^t + \phi_0^t) \quad (11b)$$

$$\text{Specular : } \phi^b = \phi^t t R_S^b + \phi_0^b \quad (12a)$$

$$\text{Lambertian : } \phi^b = 2\cos\theta \int_0^{\pi/2} \sin\theta' d\theta' (\phi^t t R_L^b + \phi_0^b) \quad (12b)$$

where the  $\theta, E$  dependence of all variables has been suppressed. We solve for  $\phi^t(\theta, E)$  and  $\phi^b(\theta, E)$  in terms of the source terms, for all four combinations of specular and Lambertian cases. The results are listed in Table I, where for simplicity of notation, we define angle-averaged transmittance with a Lambertian surface and angle av-

eraged source fluxes:

$$\mathcal{T} = \int_0^{\pi/2} \sin\theta' d\theta' 2\cos\theta' t(\theta') \quad (13)$$

$$\Phi_0^{t/b} = \int_0^{\pi/2} \sin\theta' d\theta' \phi_0^{t/b}. \quad (14)$$

## B. Current Due To Incident Photons

With the multiple-reflection problem solved, we can express  $J^{\text{in}}$  from Eq. 1. We consider illumination arriving at only the top surface, hence we take the source terms in Table I to be:

$$\phi_0^t(\theta, E) = \phi_{\text{in}}(\theta, E) [1 - R_{\text{ext}}^t(\theta, E)] \quad (15a)$$

$$\phi_0^b(\theta, E) = 0 \quad (15b)$$

where  $\phi_{\text{in}}(\theta, E)$  is the number of incident photons hitting the top surface of the cell per area per time per angle per energy,  $R_{\text{ext}}^t(\theta, E)$  is the external top surface reflectivity. In experiments, the incident flux and external reflectivity is measured in external angles, which are related to the internal angle  $\theta$  through Snell's law with a specular surface or the Lambert cosine law with a Lambertian surface. We express the incident flux and external reflectivity using internal angle for simplicity of notation, and connection to experiment requires adjusting angles accordingly. We substitute Eq. 15 into Table I and obtain the current due to incident photon absorption:

$$J^{\text{in}} = \int_{\text{hemisphere}} d\Omega \int_0^\infty dE [\phi_{\text{in}}^t + \phi_{\text{in}}^b] a \quad (16)$$

where the subscript denotes that these fluxes are due only to the incident photons and their reflections, not to any internal radiative process, which will be counted in  $J^{\text{loss}}$ .

## C. Current Due To Recombination and Photon Recycling

We calculate  $J^{\text{loss}}$  using the internal per volume emission rate and our ray-optics model to trace the reabsorption events. We calculate the  $\theta$ - and  $E$ -resolved net loss of current and integrate over solid angles and energy to obtain the total loss of current,  $J^{\text{loss}}$ . Note that for the single-layer case, this explicit ray tracing of internally emitted photons is not required, as the formulation of Green showed<sup>12</sup>. When we move to the multi-layer case, however, we must be able to track internally emitted photons and determine where they are absorbed, which requires the formalism presented here.

The  $\theta$ - and  $E$ -resolved net loss of current is divided into three parts: (1) photon flux emitted out of the cell in either up or down direction,  $\phi^r(\theta, E, \mu)$ , not including any reflections, (2) carriers lost through nonradiative recombination,  $\phi^{\text{nr}}(E, \mu)$ , and (3) recycled photons ab-

Table I. Solution of  $\phi^t$  and  $\phi^b$  from Eqs. 11 and 12. Depending on the source terms, these solutions appear in the text as  $\phi_{\text{in}}^{t/b}$  for incident photons or as  $\phi_{\text{lc}}^{t/b}$  for reflected luminescent coupling. The solution for Lambertian top and specular bottom is symmetric to the solution of specular top and Lambertian bottom, with  $t \leftrightarrow b$  exchanged

Surface Types		$\phi^t(\theta, E)$	$\phi^b(\theta, E)$
Eq. 11a,12a	Specular top	$\frac{\phi_0^b t R_S^t + \phi_0^t}{1 - t^2 R_S^t R_S^b}$	$\frac{\phi_0^t t R_S^b + \phi_0^b}{1 - t^2 R_S^t R_S^b}$
	Specular bottom		
Eq. 11b, 12b	Lambertian top	$2\cos\theta \frac{\Phi_0^b \mathcal{T} R_L^t + \Phi_0^t}{1 - \mathcal{T}^2 R_L^t R_L^b}$	$2\cos\theta \frac{\Phi_0^t \mathcal{T} R_L^b + \Phi_0^b}{1 - \mathcal{T}^2 R_L^t R_L^b}$
	Lambertian bottom		
Eq. 11a, 12b	Specular top	$2\cos\theta \frac{\int_0^{\pi/2} \sin\theta' d\theta' (\phi_0^t t R_L^b + \phi_0^b)}{1 - \int_0^{\pi/2} \sin\theta' d\theta' \cos\theta' t^2 R_S^t R_L^b} t R_S^t + \phi_0^t$	$2\cos\theta \frac{\int_0^{\pi/2} \sin\theta' d\theta' (\phi_0^t t R_L^b + \phi_0^b)}{1 - \int_0^{\pi/2} \sin\theta' d\theta' \cos\theta' t^2 R_S^t R_L^b}$
	Lambertian bottom		

sorbed after internal reflections, which enter as a negative loss,  $\phi^{\text{lc}}(E, \mu)$ . In the multi-layer case, this term will represent luminescent coupling between layers. Then,  $J^{\text{loss}}$  is

$$J^{\text{loss}}(\mu) = \int_{\text{hemisphere}} d\Omega \int_0^\infty dE \left[ 2\phi^r(\theta, E, \mu) + 2\phi^{\text{nr}}(E, \mu) - \phi^{\text{lc}}(\theta, E, \mu) \right] \quad (17)$$

Note that the factors of 2 in Eq. 17 account for both up and down propagation of photons at angle  $\theta$ , since we only integrate the solid angle over a hemisphere. From here, angular integrations are always over only a hemisphere. The three terms in Eq. 17 all depend on the internal radiative emission rate  $S^r$ , which has dimensions of number per time per volume per energy per solid angle<sup>16</sup>:

$$S^r(E, \mu) = \alpha(E) n^2(E) \frac{2}{h^3 c^2} \frac{E^2}{e^{(E-\mu)/kT} - 1} \quad (18)$$

where  $n(E)$  is the refractive index,  $h$  is Planck's constant,  $c$  is the speed of light,  $k$  is Boltzmann's constant,  $T$  is the temperature of the cell, and  $\mu$  is the quasi-Fermi level splitting in the cell. We assume that  $\mu$ ,  $T$ ,  $n$ , and  $\alpha$  are spatially uniform inside the cell, leading to spatial uniformity of  $S^r$ . Eq. 18 implies that emission events produce photons isotropically in the cell. A photon emitted upwards at angle  $\theta$  and at position  $L - z$  has a probability of  $e^{-\frac{\alpha(E)z}{\cos\theta}}$  to escape the cell, if there are no internal reflections. On integrating  $z$  from 0 to  $L$ , we obtain  $\phi^r$  in Eq. 17:

$$\phi^r(\theta, E, \mu) = \int_0^{L_i} e^{-\frac{\alpha(E)z}{\cos\theta}} S^r(E, \mu) dz \quad (19)$$

$$= \frac{\cos\theta}{\alpha(E)} a(E, \theta) S^r(E, \mu). \quad (20)$$

We define the geometry factor,  $g^r$ :

$$g^r(E, \theta) = \frac{\cos\theta}{\alpha(E)} a(E, \theta), \quad (21)$$

so  $\phi^r(\theta, E, \mu) = g^r(E, \theta) S^r(E, \mu)$ .

We include nonradiative recombination using  $\eta_{\text{int}}$ , internal radiative efficiency, which is defined as the fraction of recombination events that are radiative. In principle,  $\eta_{\text{int}}$  can depend on position and voltage, but we assume uniform and constant  $\eta_{\text{int}}$  in the cell. Then, the total nonradiative loss is proportional to  $L$  and  $S^r$ . Similar to Eq. 21, we express  $\phi^{\text{nr}}$  in Eq. 17 as  $\phi^{\text{nr}}(E, \mu) = g^{\text{nr}}(E, \theta) S^r(E, \mu)$  where

$$g^{\text{nr}}(E, \theta) = \left( \frac{1}{\eta_{\text{int}}} - 1 \right) L. \quad (22)$$

The flux of photons that are internally emitted then reflected satisfies the self-consistency relation as discussed in Section II A. We use Table I to calculate  $\phi_{\text{lc}}^t$  and  $\phi_{\text{lc}}^b$ , where the subscript indicates that the source originates from the internally emitted photons. We write the source terms as

$$\phi_0^{\text{bdy}}(\theta, E) = g^r(E, \theta) S^r(E, \mu) R^{\text{bdy}}(\theta, E) \quad (23)$$

where bdy is either t or b and  $R^{\text{bdy}}$  is specular or Lambertian reflectivity, depending on the boundary conditions chosen. Then  $\phi^{\text{lc}}$  in Eq. 17 is

$$\phi^{\text{lc}} = a(\phi_{\text{lc}}^t + \phi_{\text{lc}}^b). \quad (24)$$

We observe from Table I and Eq. 23 that both  $\phi_{\text{lc}}^t$  and  $\phi_{\text{lc}}^b$  are linear in  $S^r(E, \mu)$ , allowing writing  $\phi_{\text{lc}}$  as  $\phi_{\text{lc}} = g^{\text{lc}}(E, \theta) S^r(E, \mu)$ .

Putting these results together, we express  $J_{\text{loss}}$  using the total geometry factor,  $g(E, \theta)$ :

$$J_{\text{loss}} = \int d\Omega \int_0^\infty dE g(E, \theta) S^r(E, \mu) \quad (25)$$

where  $g(E, \theta) = 2g^r(E, \theta) + 2g^{\text{nr}}(E, \theta) + g^{\text{lc}}(E, \theta)$ , and we can now evaluate all terms in Eq. 17 for  $J^{\text{loss}}(\mu)$ . With these ideas and notation established, we now extend this formalism to a multi-layer model.

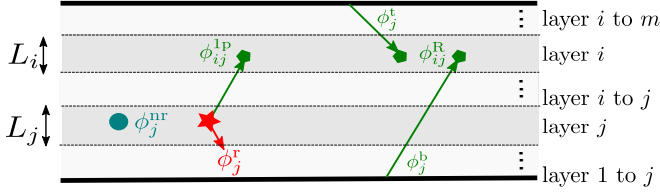


Figure 3. Reabsorption and recombination events in a multi-layer cell.

### III. MULTI-LAYER DETAILED BALANCE

As shown in Fig. 3, we consider a device with  $m$  vertically stacked layers, series connected to each other. We continue to assume infinite carrier mobility and allow each layer to have a different quasi-Fermi level splitting,  $\mu_i$ . Each layer has thickness  $L_i$ , absorption coefficient  $\alpha_i(E)$  and refractive index  $n_i(E)$ , assumed to be constant within a layer. The total device thickness is  $L = \sum L_i$ . In most III-V devices, refractive index does not vary significantly between layers, so in this work we do not include reflection or refraction between layers.

The detailed balance condition is satisfied in every layer:

$$J_i = J_i^{\text{in}} - J_i^{\text{loss}} \quad (26)$$

where  $J_i$  is the extracted current density from layer  $i$ ,  $J_i^{\text{in}}$  is the rate of absorption of incident photons per area in layer  $i$  and  $J_i^{\text{loss}}$  is the net loss of current density due to recombinations in layer  $i$ .  $J_i^{\text{loss}}$  includes LC as a negative loss.

We start with  $J_i^{\text{in}}$ . The incident photon flux in each layer is calculated similarly to the single layer case:

$$J_i^{\text{in}} = \int d\Omega \int_0^\infty dE [\phi_{\text{in}}^t t_{ti} + \phi_{\text{in}}^b t_{bi}] a_i \quad (27)$$

where we define the absorbance of each layer:

$$a_i(E, \theta) = 1 - e^{-\frac{\alpha_i(E)L_i}{\cos\theta}} \quad (28)$$

and the transmittance through all layers between but not including  $i$  and  $j$  as:

$$t_{ij}(\theta, E) = e^{-\frac{\sum_{k=i+1}^{j-1} \alpha_k(E)L_k}{\cos\theta}} \quad (29)$$

for  $i > j + 1$ , and  $t_{ji} = t_{ij}$ . Note that for  $|i - j| \leq 1$ ,  $t_{ij} = 1$ . For convenience, we define  $t_{ti}$  as transmittance through all layers above layer  $i$ ,  $t_{bi}$  as transmittance through all layers below  $i$ , and  $t_{tb}$  as the transmittance through the whole stack. In Eq. 27,  $\phi_{\text{in}}^t$  and  $\phi_{\text{in}}^b$  are calculated using Table I, with the same source terms as in Eq. 15, where we replace  $t$  with  $t_{tb}$ .

We now calculate  $J_i^{\text{loss}}$  in Eq. 26.  $J_i^{\text{loss}}$  includes three terms: (1) radiative loss,  $\phi_i^r(\theta, E, \mu_i)$ , (2) nonradiative

loss,  $\phi_i^{\text{nr}}(\theta, E, \mu_i)$ , (3) luminescent coupling (LC) from layer  $j$  to layer  $i$ ,  $\phi_{ij}^{\text{lc}}(\theta, E, \mu_j)$ . Similarly to the single-layer case in Eq. 25, we express  $J_i^{\text{loss}}$  using a geometry tensor:

$$J_i^{\text{loss}} = \int d\Omega \int_0^\infty dE \sum_{j=1}^m g_{ij}(\theta, E) S_j^r(E, \mu_j) \quad (30)$$

where  $S_j^r(E, \mu_j)$  is given by Eq. 18 with the layer-specific  $\alpha_i(E)$ ,  $n_i(E)$ , and  $\mu_i$ . In PPC's, all  $\alpha_i$  and  $n_i$  are the same in every layer, but we include the possibility of varying  $\alpha$  and  $n$  to include the case of solar cells, in which each layer can have different material properties.

We proceed to calculate the geometry tensor. Similarly to the single layer model,

$$g_{ij}(E, \theta) = 2\delta_{ij}g_{ij}^r(E, \theta) + 2\delta_{ij}g_{ij}^{\text{nr}}(E, \theta) - g_{ij}^{\text{lc}}(E, \theta) \quad (31)$$

where  $\delta_{ij}$  is the Kronecker delta. Analogous to Eqs. 21 and 22, the radiative and nonradiative geometry factors in each layer are:

$$g_i^r(E, \theta) = \frac{\cos\theta}{\alpha_i(E)} a_i(E, \theta) \quad (32)$$

$$g_i^{\text{nr}}(E, \theta) = \left( \frac{1}{\eta_{\text{int}}^i} - 1 \right) L_i \quad (33)$$

We divide the LC term,  $g^{\text{lc}}(\theta, E)$ , into one-pass and after-reflection contributions:

$$g_{ij}^{\text{lc}} = g_{ij}^{\text{1p}} + g_{ij}^{\text{R}}. \quad (34)$$

Without reflection, the geometry factor is

$$g_{ij}^{\text{1p}} = (1 - \delta_{ij}) a_i t_{ij} g_j^r, \quad (35)$$

where we use  $(1 - \delta_{ij})$  because one-pass reabsorption within the same layer is already included in  $g_i^r$ . We obtain  $\phi_{ij}^{\text{R}} = g_{ij}^{\text{R}} S_j^r$  from the self-consistent reflected fluxes at the top and bottom surfaces from Table I. For radiative events occurring in layer  $j$ , we take the source terms to be:

$$\phi_0^{\text{bdy}} = g_j^r S_j^r t_{j\text{bdy}} R^{\text{bdy}}, \quad (36)$$

where bdy is t or b, and find  $\phi_j^{\text{bdy}}$  from Table I. Then the absorption in layer  $i$  from radiative events in layer  $j$  is:

$$\phi_{ij}^{\text{R}} = a_i (\phi_j^t t_{ti} + \phi_j^b t_{bi}). \quad (37)$$

Using Eqs. 27 and 30 to 37, we obtain  $J_i$  in Eq. 26. When all layers are series connected, they share the same current density,  $J_i = J$ , which depends on the set of quasi-Fermi levels,  $\mu_i$ . At one  $J$  value, we can solve for a set of  $\mu_i$  values, the sum of which gives the voltage of

the device. The efficiency is then written in terms of  $J$ :

$$\eta(J) = \frac{J \sum_i \mu_i(J)}{P_{\text{in}}} \quad (38)$$

Optimizing with respect to  $J$  gives the maximum efficiency.

#### IV. EFFICIENT COMPUTATION OF $V(J)$

Finding  $\eta(J)$  involves solving Eq. 26 with  $J_i = J$ , which is a system of  $m$  nonlinear equations in  $\mu_i$ , and is computationally challenging. We can significantly reduce the computational cost by making simplifying assumptions on  $\alpha(E)$  and the top and bottom reflectivities. First, we rewrite Eq. 26 using Eq. 30:

$$J_i = J_i^{\text{in}} - \int d\Omega \int_0^\infty dE \left[ \sum_{j=1}^m g_{ij}(\theta, E) S_j^r(E, \mu_j) \right]. \quad (39)$$

We can simplify the calculation of  $J(V)$  if (1)  $\alpha_i(E)$  is zero for  $E$  less than the band gap  $E_g^i$  and a constant for  $E > E_g^i$  and (2) top and bottom reflectivity are independent of  $E$ . In this case,  $g_{ij}(\theta, E)$  becomes  $g_{ij}(\theta)$  for all  $E > E_g^i$ , allowing the angular integral to be separated from the energy integral. Then we can rewrite Eq. 39 as:

$$J_i = J_i^{\text{in}} - \sum_{j=1}^m G_{ij} \mathcal{R}_j(\mu_j) \quad (40)$$

where

$$G_{ij} = \int d\Omega g_{ij}(\theta) \quad (41)$$

$$\mathcal{R}_j(\mu_j) = \int_{E_g^j}^\infty dE S_j^r(E, \mu_j). \quad (42)$$

Eq. 40 is a linear system of equations with unknowns  $\mathcal{R}_j$ . Thus for fixed  $J$  we can efficiently solve for  $\mathcal{R}_j$ . We then invert  $\mathcal{R}_j$  to find  $\mu_j$ , using Eqs. 18 and 42, which allows us to find the external bias  $V = \sum_i \mu_i$ . We thus calculate  $V(J)$  instead of  $J(V)$ . Either way, the power output is  $JV$ , and the maximum power point can be found numerically.




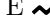

#### V. APPLICATION: MULTILAYER MONOCHROMATIC CONVERSION

In this section, we demonstrate the use of this model by considering a set of monochromatic devices inspired by the record-efficiency PPC device but with  $m$  vertically stacked layers, varied  $\eta_{\text{int}}$ , and top and bottom boundary conditions. The effects of input power density, wavelength, linewidth, external radiative efficiency, which is different from  $\eta_{\text{int}}$ , absorbance and band gap were previ-

Table II. Fixed parameters for Section V

Property	Value
Band gap $E_g^{19}$	1.424 eV
Absorption Coefficient $\alpha^{19}$	$1.151 \times 10^6$ /m
Input Intensity	$8 \times 10^4$ W/m <sup>2</sup>
Input Wavelength	830 nm (1.494 eV)
Input Linewidth	1 nm
Series Resistance	0

Table III. Top and bottom reflectivity configurations considered in this section along with icons to identify each combination.

Bottom \ Top	Total internal reflection	Lambertian
	Absorbing substrate	A 
Specular mirror	C 	D 
Lambertian mirror	E 	F 

ously studied in a single-layer model<sup>12,17</sup> and with only one boundary condition in a multi-layer model<sup>18</sup>. Here we fix those parameters as in Table II to approximate the record-efficiency PPC<sup>11</sup>. We show that devices with an absorbing substrate can improve their efficiency by increasing the number of layers, even without series resistance. This effect does not exist with a back reflector, which shows no improvement with increased number of layers. In Section VI we present a simple model to explain these effects.

#### A. Reflectivity Models

For these examples, we consider a set of simple reflectivity models to approximate different levels of light trapping. We only consider models that are angle-dependent but not  $E$ -dependent to reduce computational costs, as discussed in Section IV. The general model of Section III allows any reflectivity configuration with dependence on  $\theta$  and  $E$ .

We consider two models for the internal reflectivity at the top interface. In the following discussion, the top surface is an interface between air ( $n_{\text{air}} = 1$ ) and a material with index  $n$ . We consider perfect transmission of external light into the sample, but there must be total internal reflection of optical modes on the inside surface. In the "Total internal reflection" model, we consider specular reflection of all incident rays with  $\theta > \theta_c$ , so  $R_S^t(\theta)$  is a step function that is zero for  $\theta < \theta_c$ , and one for all larger angles. As usual, the critical angle is  $\theta_c = \sin^{-1}(n_{\text{air}}/n)$ . The second top surface we consider is an ideal Lambertian surface, which randomizes the angle of propagation for reflected and transmitted photons. An ideal Lambertian surface admits all incident photons into the cell from the exterior while reflecting internal photons with

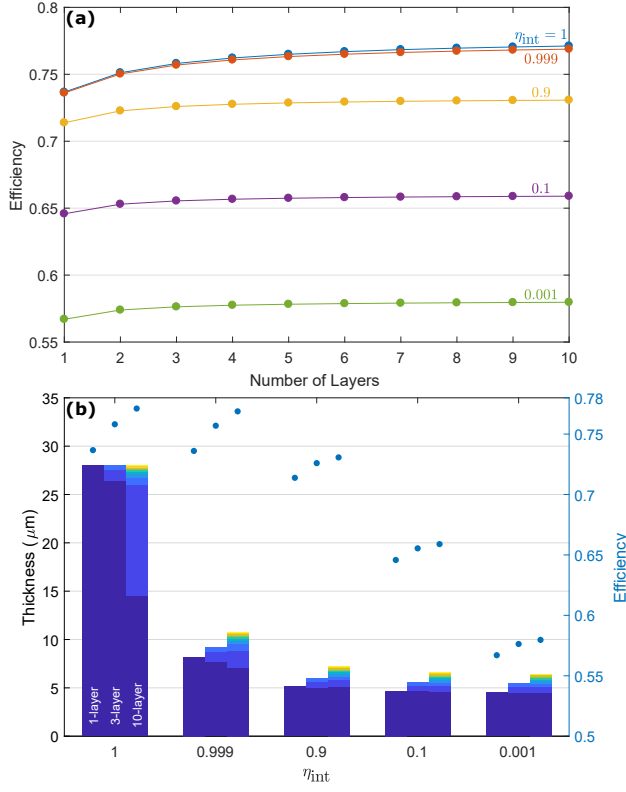


Figure 4. (a) Efficiency, optimized with respect to layer thicknesses, as a function of number of layers with Configuration A in Table II for several values of  $\eta_{\text{int}}$ . (b) Optimal layer thicknesses of 1-, 3- and 10-layer cells (left axis, bars) and the associated efficiencies (right axis, points).

a probability of  $1 - \frac{n_{\text{air}}^2}{n^2}$ .

At the bottom surface, we consider three surface models. In the case of an absorbing substrate, we consider all photons hitting the bottom surface to be lost, i.e.,  $R_S^b = 0$  for all angles. A specular mirror reflects all photons back into the cell at the same angle as incidence, i.e.,  $R_S^b = 1$  for all angles. A Lambertian mirror also reflects all photons back into the cell but at a random angle of reflection.

We consider all six combinations of these models for the top and bottom surface reflectivities, as listed in Table III. We label the six scenarios from A to F and also include an icon for each scenario.

## B. Intrinsic Efficiency Increase With Number of Layers

We first consider Configuration A in Table III, which has no light trapping and best represents the device of Ref.<sup>11</sup>. We numerically optimize the layer thicknesses to maximize efficiency with  $\eta_{\text{int}}$  values of 1, 0.999, 0.9, 0.1, 0.001. These values of  $\eta_{\text{int}}$  represent material qualities ranging from the radiative limit to low quality. In the radiative limit ( $\eta_{\text{int}} = 1$ ), the optimal thickness of the full

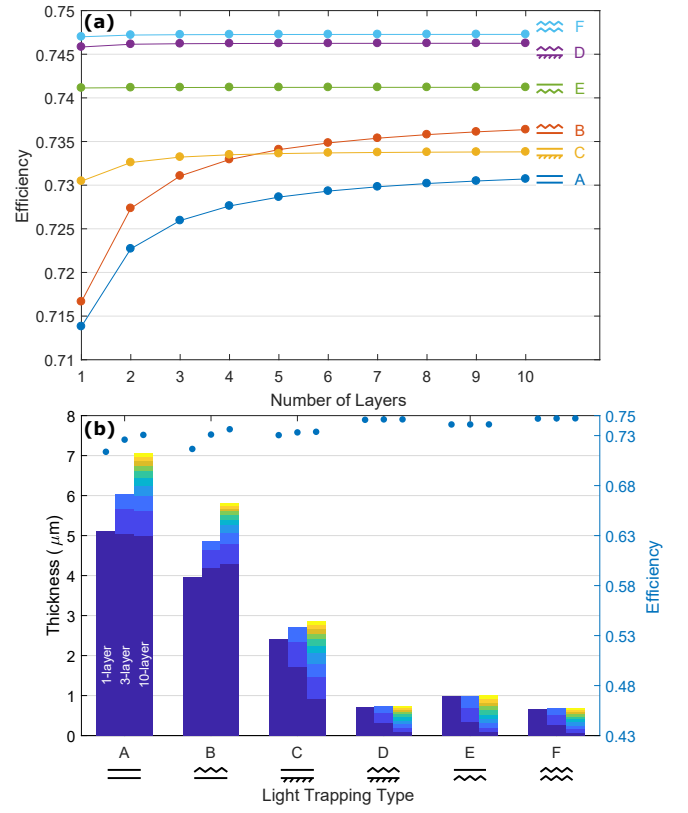


Figure 5. (a) Efficiency, optimized with respect to layer thicknesses, as a function of number of layers for all 6 surface configurations in Table III.  $\eta_{\text{int}} = 0.9$ . Note that A, B have substrates and show the strongest intrinsic efficiency increase with  $m$ . (b) Optimal layer thicknesses of 1-, 3- and 10-layer stack.

device is infinity so the cell absorbs all incident photons. Since nonradiative loss scales as  $\left(\frac{1}{\eta_{\text{int}}} - 1\right)L$ , there is a trade-off between nonradiative recombination loss and transparency loss when  $\eta_{\text{int}} < 1$ , giving a finite optimal device thickness. Hence, we optimize layer thicknesses without a constraint on total thickness for all  $\eta_{\text{int}} < 1$  cases, while in the case of  $\eta_{\text{int}} = 1$ , we constrain the total thickness to have a vertical one pass absorbance of  $1 - e^{-\alpha L} = 1 - 10^{-14}$ .

The key results are shown in Fig. 4, giving the optimized efficiencies and layer thicknesses for a range of  $\eta_{\text{int}}$  and  $m$ . As expected, efficiency decreases as  $\eta_{\text{int}}$  decreases. More surprisingly, for all  $\eta_{\text{int}}$  values, efficiency increases with the number of layers. In the radiative limit, efficiency increases by 3.4% abs. from 1 to 10 layers; at  $\eta_{\text{int}} = 0.001$ , efficiency increases by 1.3% abs. Efficiency is expected to improve in multi-layer devices with series resistance, as the devices increase voltage while decreasing current and its associated losses. In this case, however, we see an improvement of efficiency even without series resistance.

We show in Fig. 5 efficiency at optimal layer thick-

nesses for all 6 surface configurations in Table III. Material quality is fixed at  $\eta_{\text{int}} = 0.9$ , which represents high-quality III-V materials. Among all configurations, case A has the lowest efficiency, because this configuration does not include any light trapping. Efficiency is highest in Case F with two ideal Lambertian surfaces. Only cases with absorbing substrate (A and B) show strong efficiency increase with increasing  $m$ .

A back reflector and light trapping are helpful for PPC efficiency. The record-efficiency device, however, is on a thick GaAs substrate with a full metal contact<sup>11,20</sup>. Since the GaAs substrate is absorbing and optically thick, this architecture is equivalent to an absorbing substrate without a back reflector. In such a system, this intrinsic increase of efficiency with  $m$  is an intriguing route to high efficiency, which reinforces the simpler series-resistance advantages of multi-layer devices. In order to understand the physical origin of this increased efficiency, we present a toy model of a 1- and 2-layer device, with and without a back reflector.

## VI. 2-LAYER MODEL

In this section, we reduce our full model from Section III, to a semi-analytic 2-layer model. Using this simplified model, we demonstrate that the multi-layer device allows radiative losses into the substrate to be reduced, but that no equivalent improvement can be obtained when there is a back reflector. We consider Configurations B and F in Table III. The simplest expectation for  $m = 1$  devices is that the operating current is  $J_{\text{mp}}^{(1)} \simeq J^{\text{in}}$ , and we call the operating voltage  $V_{\text{mp}}^{(1)}$ . With  $m > 1$ , one might expect that  $J_{\text{mp}}^{(m)} \simeq J_{\text{mp}}^{(1)}/m$  and that each layer keeps the same voltage as in the one-layer device, giving a total voltage of  $V_{\text{mp}}^{(m)} \simeq mV_{\text{mp}}^{(1)}$ , which would give no change in the efficiency (in the absence of series resistance). For Configuration B in Fig. 5(a), however, we see a 1.5% (rel.) increase in efficiency on moving from  $m = 1$  to  $m = 2$ . In these devices,  $mJ_{\text{mp}}^{(m)}$  changes by only 0.26%, so the more significant increase in efficiency comes from the operating voltage.

There is no analytic solution to  $V_{\text{mp}}^{(m)}$  and  $J_{\text{mp}}^{(m)}$ . Hence, for qualitative understanding, we study the the short-circuit current  $J_{\text{sc}}^{(m)}$  and the open-circuit voltage  $V_{\text{oc}}^{(m)}$ , as well as the product  $J_{\text{sc}}^{(m)}V_{\text{oc}}^{(m)}$ . We choose configurations with Lambertian surfaces in order to express the emission and absorption flux using the same angle-averaged absorbance. For the same reason, we assume that there is a filter between two layers that randomizes the the angle of the transmitted light. We work in the radiative limit and consider  $n = 1$ , so there is no reflection at cell-air or cell-substrate interfaces. We assume that absorption coefficient is 0 for energy lower than the band gap, and constant  $\alpha$  for energy above the band gap. For simplicity, we work in the Boltzmann approximation, in which the “-1” in the denominator of Eq. 18 is neglected, which

is valid when the internal cell voltages do not get within a few  $kT$  of  $E_g$ . The detailed-balance condition, Eq. 39, for each layer is then

$$J_1 = J^{\text{in}}(1 - A_2)A_1[1 + R_L^{\text{b}}(1 - A_1)] \quad (43a)$$

$$- J_0e^{V_1}(2A_1 - R_L^{\text{b}}A_1^2) + J_0e^{V_2}A_2[A_1 + R_L^{\text{b}}(1 - A_1)A_1]$$

$$J_2 = J^{\text{in}}A_2[1 + R_L^{\text{b}}(1 - A_2)(1 - A_1)^2] \quad (43b)$$

$$- J_0e^{V_2}[2A_2 - R_L^{\text{b}}A_2^2(1 - A_1)^2] + J_0e^{V_1}(2A_1 - R_L^{\text{b}}A_1^2)A_2,$$

where  $A$  is the angle-averaged one-pass absorbance:

$$A = \frac{\int_0^{\pi/2} (1 - e^{-\frac{\alpha L}{\cos\theta}}) \cos\theta \sin\theta d\theta}{\int_0^{\pi/2} \cos\theta \sin\theta d\theta} \quad (44)$$

and  $J_0$  is short-circuit radiative recombination current in one of the up or down direction:

$$J_0 = \frac{2\pi}{h^3 c^2} \int_{E_g}^{\infty} dE E^2 e^{-E/kT}. \quad (45)$$

The top layer absorbs the incident radiation,  $A_2 J^{\text{in}}$ , in one-pass, and  $R_L^{\text{b}}(1 - A_2)(1 - A_1)^2 A_2 J^{\text{in}}$ , in the second pass, where  $R_L^{\text{b}}$  is the back reflectivity. The top layer radiates both out the top surface and to the bottom layer ( $J_0 e^{V_2} A_2$ ). The top layer has luminescent coupling from the bottom layer (proportional to  $J_0 e^{V_1} A_1$ ) as well as photon recycling due to the back reflector. The bottom layer receives the filtered incident radiation  $(1 - A_2)A_1 J^{\text{in}}$  in one pass,  $R_L^{\text{b}}(1 - A_2)(1 - A_1)A_1 J^{\text{in}}$  in the second pass, luminescent coupling in two passes from the top layer (proportional to  $J_0 e^{V_2} A_2$ ), and also has radiative emission to the top layer and the substrate. We can recover a 1-layer detailed balance model by setting either  $A_1$  or  $A_2$  to be zero. For simplicity of notation, we delete the subscript when referring to the 1-layer quantities. Using Eq. 43, we study the cases of  $R_L^{\text{b}} = 0$ , absorbing substrate, and  $R_L^{\text{b}} = 1$ , ideal back reflector.

Starting with a 1-layer device, we solve for  $V_{\text{oc}}$  and  $J_{\text{sc}}$  in Eq. 43 in each of the two cases:

$$\frac{V_{\text{oc}}^{(1)}}{kT} = \begin{cases} \ln \tilde{J} + \ln \frac{1}{2} & \text{substrate} \\ \ln \tilde{J} & \text{back reflector} \end{cases} \quad (46)$$

$$\tilde{J}_{\text{sc}}^{(1)} = \begin{cases} A(\tilde{J} - 2) & \text{substrate} \\ (2A - A^2)(\tilde{J} - 1) & \text{back reflector} \end{cases} \quad (47)$$

where  $\tilde{J} = \frac{J^{\text{in}}}{J_0}$  and  $\tilde{J}_{\text{sc}} = \frac{J_{\text{sc}}}{J_0}$ .

In 2-layer devices, the voltage of each layer at open



circuit is:

$$\frac{V_{\text{oc},1}^{(2)}}{kT} = \begin{cases} \ln \tilde{J} + \ln \frac{(2-A_2)}{4-A_1A_2} & \text{substrate} \\ \ln \tilde{J} & \text{back reflector} \end{cases} \quad (48)$$

$$\frac{V_{\text{oc},2}^{(2)}}{kT} = \begin{cases} \ln \tilde{J} + \ln \frac{(2+A_1-A_1A_2)}{4-A_1A_2} & \text{substrate} \\ \ln \tilde{J} & \text{back reflector} \end{cases} \quad (49)$$

For a two-layer device at short-circuit: (1)  $J_{\text{sc}} = J_1 = J_2$ , and (2)  $V_1 + V_2 = 0$ . Solving Eq. 43 with these constraints, we obtain the short-circuit current. Due to the length of the general solution, here we present only the solution evaluated at  $A_1 = 1$  and  $A_2 = 1/2$ , which we consider further below:

$$\tilde{J}_{\text{sc}}^{(2)} = \begin{cases} \frac{\tilde{J}}{2} - \frac{7}{2\sqrt{15}} & \text{substrate} \\ \frac{\tilde{J}}{2} - \frac{1}{2} & \text{back reflector} \end{cases} \quad (50)$$

To understand the origin of the efficiency improvement with  $m$ , we compare the value of  $V_{\text{oc}}^{(m)}/m$  and  $J_{\text{sc}}^{(m)}m$ , as well as the product of the two quantities. Since,  $0 \leq A_i \leq 1$ , with a substrate we always have  $V_{\text{oc},1}^{(2)} \leq V_{\text{oc}}^{(1)} \leq V_{\text{oc},2}^{(2)}$ . The average  $V_{\text{oc}}^{(2)}$  with substrate can be larger or smaller than  $V_{\text{oc}}^{(1)}$ , depending on the values of  $A_1$  and  $A_2$ . We consider absorption-matched devices with infinite thickness for  $m = 1, 2$ . In this case,  $A = 1$  for the 1-layer case, and  $A_1 = 1$  and  $A_2 = 1/2$  with 2 layers. Here, both the single- and 2-layer devices absorb all incident photons. In the case of an absorbing substrate, the per-layer  $V_{\text{oc}}$  of the 2-layer device is strictly larger than that of the 1-layer device. Specifically, for  $\tilde{J} = 10$ , the average 2-layer  $V_{\text{oc}}$  is 6.3% higher than the 1-layer  $V_{\text{oc}}$ . At the same time,  $mJ_{\text{sc}}^{(m)}$  also increases by 2.4%. We thus see that the efficiency with  $m = 2$  is larger than with  $m = 1$ , due to increases in both  $J_{\text{sc}}$  and  $V_{\text{oc}}$ , though the  $V_{\text{oc}}$  increase is more significant. The product,  $J_{\text{sc}}^{(m)}V_{\text{oc}}^{(m)}$ , increases by 8.8%.

In the case of a substrate, the voltage difference between the top and bottom layers reduces radiative loss to the substrate. Radiative losses from the top surface are inevitable, as the device must be able to admit incident radiation. Radiative losses out the rear of the device, however, are pure losses. In a single-layer device, those losses are unavoidable at any voltage. The multi-layer device is able to reduce the impact of those losses by decreasing the internal voltage of the bottom layer, which reduces the radiation into the substrate, while allowing the upper layer to maintain a larger internal voltage. Reduced radiative loss out the bottom layer also increases the collected current  $mJ_{\text{sc}}$ , but this effect is smaller.

Interestingly, at higher incident flux density, both  $V_{\text{oc}}$  and  $J_{\text{sc}}$  effects are weaker. The power density used in Section V corresponds to  $\tilde{J} \approx 9 \times 10^{16}$ . With this value, in the toy model  $V_{\text{oc}}^{(m)}/m$  increases by 0.26%, while  $mJ_{\text{sc}}^{(m)}$  stays the same within machine precision. In the full model of Section III with  $n = 1$  and  $\eta_{\text{int}} = 1$ , the im-

provement of maximum power on moving from  $m = 1$  to  $m = 2$  for Configuration B is 0.22%, in good agreement with the simpler model. With GaAs refractive index,  $n = 3.64$ , the improvement is 2.0%, similar to that shown in Fig. 5(a), showing that the increased top-surface light trapping increases the importance of this effect.

In contrast, for the case with a back reflector, the voltage of each layer in a 2-layer device is analytically equal to the voltage of the single-layer device in all  $A_1$  and  $A_2$  values. And  $2J_{\text{sc}}^{(2)}$ , evaluated at the absorption matched case of  $A_1 = 1$  and  $A_2 = 1/2$ , is also analytically equal to  $J_{\text{sc}}^{(1)}$  at  $A = 1$ . This matches our observation in the full model that efficiency does not increase with number of layers in Configuration F.

The highly nonradiative case,  $\eta_{\text{int}} \ll 1$ , is also amenable to analytic treatment and shows a similar increase of efficiency with  $m$ .

We have generalized monochromatic detailed balance models<sup>12,17</sup> to multi-layer devices, including: (1) bi-directional luminescent coupling, (2) nonradiative recombination parametrized by  $\eta_{\text{int}}$ , (3) mixed specular and Lambertian surface reflection. We observe an intrinsic increase of efficiency with number of layers, independent of series resistance, for PPC's on absorbing substrates. This intrinsic increase is not present when the device has a back reflector. Other than the well-known benefits of multi-layer PPC's, such as high voltage and low series resistance, we have discovered another mechanism for efficiency increase with number of layers, which further encourages future multi-layer designs of PPCs.

## ACKNOWLEDGEMENT

We acknowledge helpful conversations with Matthew M. Wilkins. This work was supported by NSERC grant number STPGP 494090 and Ontario Early Researcher Award ER17-13-019. The data that support the findings of this study are available from the corresponding author upon reasonable request.

## REFERENCES

- <sup>1</sup>M. A. Steiner, J. F. Geisz, I. Garca, D. J. Friedman, A. Duda, W. J. Olavarria, M. Young, D. Kuciauskas, and S. R. Kurtz, "Effects of Internal Luminescence and Internal Optics on  $v_{\text{oc}}$  and  $j_{\text{sc}}$  of III-V Solar Cells," *IEEE Journal of Photovoltaics* **3**, 1437–1442 (2013).
- <sup>2</sup>D. J. Friedman, J. F. Geisz, and M. A. Steiner, "Effect of Luminescent Coupling on the Optimal Design of Multijunction Solar Cells," *IEEE Journal of Photovoltaics* **4**, 986–990 (2014).
- <sup>3</sup>J. F. Geisz, M. A. Steiner, I. Garca, R. M. France, W. E. McMahon, C. R. Osterwald, and D. J. Friedman, "Generalized Optoelectronic Model of Series-Connected Multijunction Solar Cells," *IEEE Journal of Photovoltaics* **5**, 1827–1839 (2015).
- <sup>4</sup>C. Baur, M. Hermle, F. Dimroth, and A. W. Bett, "Effects of optical coupling in III-V multilayer systems," *Applied Physics Letters* **90**, 192109 (2007).

- <sup>5</sup>N. L. A. Chan, T. Thomas, M. Fhrer, and N. J. Ekins-Daukes, “Practical Limits of Multijunction Solar Cell Performance Enhancement From Radiative Coupling Considering Realistic Spectral Conditions,” *IEEE Journal of Photovoltaics* **4**, 1306–1313 (2014).
- <sup>6</sup>M. Wilkins, C. E. Valdivia, A. M. Gabr, D. Masson, S. Fafard, and K. Hinzer, “Luminescent coupling in planar opto-electronic devices,” *Journal of Applied Physics* **118**, 143102 (2015).
- <sup>7</sup>A. W. Setiawan Putra, M. Tanizawa, and T. Maruyama, “Optical Wireless Power Transmission Using Si Photovoltaic Through Air, Water, and Skin,” *IEEE Photonics Technology Letters* **31**, 157–160 (2019).
- <sup>8</sup>M. M. Wilkins, M. Ishigaki, P. Provost, D. Masson, S. Fafard, C. E. Valdivia, E. M. Dede, and K. Hinzer, “Ripple-Free Boost-Mode Power Supply Using Photonic Power Conversion,” *IEEE Transactions on Power Electronics* **34**, 1054–1064 (2019).
- <sup>9</sup>A. Basanskaya, “Electricity over glass,” *IEEE Spectrum* **42**, 18–(2005).
- <sup>10</sup>M. Roeger, G. Bttger, M. Dreschmann, C. Klamouris, M. Huebner, A. Bett, J. Becker, W. Freude, and J. Leuthold, “Optically powered fiber networks,” *Optics express* **16**, 21821–34 (2009).
- <sup>11</sup>S. Fafard, M. C. A. York, F. Proulx, C. E. Valdivia, M. M. Wilkins, R. Ars, V. Aimez, K. Hinzer, and D. P. Masson, “Ultrahigh efficiencies in vertical epitaxial heterostructure architectures,” *Applied Physics Letters* **108**, 071101 (2016).
- <sup>12</sup>M. A. Green, “Limiting photovoltaic monochromatic light conversion efficiency,” *Progress in Photovoltaics: Research and Applications* **9**, 257–261 (2001).
- <sup>13</sup>W. Shockley and H. J. Queisser, “Detailed Balance Limit of Efficiency of  $p$ - $n$  Junction Solar Cells,” *Journal of Applied Physics* **32**, 510–519 (1961).
- <sup>14</sup>J. Balenzategui and A. Mart, “Detailed modelling of photon recycling: application to GaAs solar cells,” *Solar Energy Materials and Solar Cells* **90**, 1068–1088 (2006).
- <sup>15</sup>M. A. Green, “Lambertian light trapping in textured solar cells and light-emitting diodes: analytical solutions,” *Progress in Photovoltaics: Research and Applications* **10**, 235–241 (2002).
- <sup>16</sup>P. Wurfel, “The chemical potential of radiation,” *Journal of Physics C: Solid State Physics* **15**, 3967–3985 (1982).
- <sup>17</sup>D. Xia, M. M. Wilkins, S. S. Chahal, C. E. Valdivia, K. Hinzer, and J. J. Krich, “Opportunities for Increased Efficiency in Monochromatic Photovoltaic Light Conversion,” in *2018 IEEE 7th World Conference on Photovoltaic Energy Conversion (WCPEC)* (2018) pp. 3688–3692.
- <sup>18</sup>D. Xia, M. N. Beattie, M. Chun Tam, M. M. Wilkins, C. E. Valdivia, Z. R. Wasilewski, K. Hinzer, and J. J. Krich, “Opportunities for High Efficiency Monochromatic Photovoltaic Power Conversion at 1310 nm,” in *2019 IEEE 46th Photovoltaic Specialists Conference (PVSC)* (2019) pp. 2303–2306.
- <sup>19</sup>S. Adachi, *Optical constants of crystalline and amorphous semiconductors: numerical data and graphical information* (Kluwer Academic Publishers, Boston, 1999).
- <sup>20</sup>D. Masson, F. Proulx, and S. Fafard, “Pushing the limits of concentrated photovoltaic solar cell tunnel junctions in novel high-efficiency GaAs phototransducers based on a vertical epitaxial heterostructure architecture,” *Progress in Photovoltaics: Research and Applications* **23**, 1687–1696 (2015).